Novel Nanoparticles with Cr^{3+} Substituted Ferrite for Self-regulating Temperature Hyperthermia †

Wei Zhang,[a] Xudong Zuo,[a] Ying Niu,[a] Chengwei Wu,[*a] Shuping Wang,[b] Shui Guan[b] and S. Ravi P. Silva[*c]

For hyperthermia to be used under clinical conditions for cancer therapeutics the temperature regulation needs to be precise and accurately controllable. In the case of the metal nanoparticles used for such activities, a high coercivity is a prerequisite in order to couple more energy in a single heating cycle for efficient and faster differential heating. The chemically stable Co-Zn ferrite nanoparticles have typically not been used in such self-regulating temperature hyperthermia applications to date due to their low Curie temperature usually accompanied with a poor coercivity. The latter physical property limitation under clinically applied magnetic field conditions (frequency: 100 kHz, intensity: 200 Oe) restricts the transfer of a reasonable heat energy, and thus limits the hyperthermia efficiency. Here, we report a novel Cr^{3+} substituted Co-Zn ferrite ($Zn_{0.54}Co_{0.46}Cr_{0.6}Fe_{1.4}O_4$), whose Curie temperature and coercivity values are 45.7°C and 174 Oe, respectively. Under clinically acceptable magnetic field conditions, the temperature of these nanoparticle suspensions can be self-regulated to 44.0°C and, most importantly with a specific absorption rate (SAR) of 774 W kg^{-1}, which is two folds higher than the SAR standard for magnetic nanoparticles used in hyperthermia (300 W kg^{-1}). The evaluation of the in vitro cytotoxicity of the nanoparticles reports a low toxicity, which points to a novel set of magnetic nanoparticles for use in self-regulating hyperthermia.

Introduction

Magnetic induction hyperthermia is considered as an accurate, efficient and green method for treating malignant tumors. [1] It is part of the drive to use nanobiotechnology for the accurate targeting and precise delivery of treatments to cancers that circumvents large doses of typically toxic drugs that can have major side effects. [2-4] Basically, magnetic media are introduced to the tumor region by implantation or intervention and will generate heat upon the application of local external alternating magnetic field. Since normal cells possess higher heat resistance and resilience than tumor cells, the tumor cells can be killed without affecting normal tissue if the temperature can be maintained accurately to within 42°C-45°C.[5-7]

As monitoring hyperthermia temperature in vivo with minimal invasion is still a challenge, magnetic media with low Curie temperature, in particular at the hyperthermia temperature range of 42-45°C, are highly desired. [8-12] The Curie temperature is the temperature at which ferromagnetic materials lose their intrinsic permanent magnetic properties and consequently lose their ability of aligning to external fields and thus facilitating the conversion of external electromagnetic energy into highly localized heat. The Curie temperature therefore gives an upper limit to the operational temperature for the magnetic media. The ability to tune the Curie temperature to a value just above the treatment temperature would be an expedient route to control the hyperthermia temperature and realize self-regulation in practical use of magnetic media as both heater and fuse-limiter. [13]

To minimize any collateral effects of alternating magnetic fields to the human body, the frequency and intensity of the magnetic field in clinical treatment should not be higher than 100 kHz and 200 Oe, respectively. [14] The coercivity (H_c) of the magnetic media is considered a key parameter which significantly influences the heat transfer efficiency from the alternating magnetic field to the human cells. When H_c is higher than the intensity of alternating magnetic field, the saturated hysteresis loops cannot be completely used to generate heat. As the unsaturated loops are then virtually used to generate heat, the heating efficiency is reduced precipitously. If H_c is much lower than the intensity of alternating magnetic field, although fully saturated hysteresis loops are used, the small area of the hysteresis loops will still lead to lower heat generation efficiency. [15] Clearly, to achieve a high heating efficiency, the H_c of the magnetic media should approach the clinically safety intensity threshold (200 Oe) of the alternating magnetic field as closely as possible.

One of the most widely used magnetic media for hyperthermia is Co-Zn ferrite nanoparticles. [16-19] These nanoparticles with spinel structure possess high chemical stability which is suitable for hyperemia in the complex human body environments. Besides the

[a]State Key Laboratory of Structural Analysis for Industrial Equipment, Department of Engineering Mechanics, Dalian University of Technology, Dalian 116024, P. R. China. Email: cwwu@dlut.edu.cn
[b]School of Chemical Engineering, Dalian University of Technology, Dalian 116024, P. R. China.
[c]Advanced Technology Institute, University of Surrey, Guildford, Surrey GU2 7XH, U.K. Email: s.silva@surrey.ac.uk
†Electronic supplementary information available: Table S1-The theoretical and measured element ratios of nanoparticles, Figure S1-Arulmurugan's results and its linear fitted curve.

Curie temperature and H_c, these nanoparticles can be tuned by changing the element ratio of Co and Zn, which makes it possible to achieve reasonable heat efficiency and hyperthermia temperatures. However, the substituting of non-magnetic Zn^{2+} with magnetic Co^{2+} will cause the reduction of super-exchange interaction strength and magnetocrystalline anisotropy in sub-lattices, resulting in a decrease of the Curie temperature and H_c simultaneously. For instance, when the Curie temperature of Co-Zn ferrite nanoparticles is below 285°C, their H_c is as low as 10 Oe. [20] This indicates Co-Zn ferrite nanoparticles are not impossible, but quite unlikely, to be used in hyperthermia with the self-regulating characteristic as the low Curie temperature (45°C) is often accompanied by low heating efficiency.

In our previous work, we found that substituting Fe^{3+} by non-magnetic Cr^{3+} in the spinel ferrite nanoparticles can decrease the Curie temperature and increase H_c simultaneously, which is attributed to the effect of Cr^{3+} on the spinel structure of ferrite in the formation process of nanoparticles. [21-23] In addition, the analogous valence-bond structure and similar radius of Fe^{3+} and Cr^{3+} makes their amorphous hydroxide precipitates behave thermodynamically to true solid solutions and consequently the Cr^{3+} may be substituted into Co-Zn ferrite without breaking its spinel lattice structure and symmetry. [24] Theoretically, substituting Cr^{3+} into Co-Zn ferrite nanoparticles provides the possibility for optimizing the Curie temperature and H_c to 45°C and 200 Oe simultaneously. In this communication, a certain quantity of Cr^{3+} was substituted into Co-Zn ferrite, $Zn_xCo_{1-x}Cr_{0.6}Fe_{1.4}O_4$ (x=0, 0.2, 0.4, 0.54, 0.56) nanoparticles with the Curie temperature ranging from 361°C to 35°C and H_c ranging from 6400 Oe to 107 Oe were obtained. Among them, the Curie temperature and H_c of $Zn_{0.54}Co_{0.46}Cr_{0.6}Fe_{1.4}O_4$ nanoparticles reach 45.7°C and 174 Oe respectively. The self-regulating temperature of $Zn_{0.54}Co_{0.46}Cr_{0.6}Fe_{1.4}O_4$ nanoparticle suspension is close to the hyperthermia temperature (around 44.0°C) and its specific absorption rate (SAR) is 774 W kg^{-1} which is two folds higher than the SAR standard for magnetic nanoparticles used in hyperthermia, [25] under magnetic field with the frequency and intensity at 100 kHz and 200 Oe. In addition, the evaluation of in vitro cytotoxicity of $Zn_{0.54}Co_{0.46}Cr_{0.6}Fe_{1.4}O_4$ nanoparticles was also performed and no obvious toxicity effects were observed in this study. This study proposes a methodology for the first time on the bespoke synthesis of magnetic nanoparticles for self-regulating hyperthermia.

Experimental

Chemical synthesis

$FeCl_3 \cdot 6H_2O$ (99%+) and $CrCl_3 \cdot 6H_2O$ (99%+) were obtained from Shantou Xilong Chemical Co. Ltd., China. $CoCl_2 \cdot 6H2O$ (99%+) and NaOH (96%+) were supplied by Tianjin Bodi Chemical Co. Ltd., China. $ZnCl_2$ (98%+) was supplied by Tianjin Damao Chemical Co. Ltd., China. $CrCl_3 \cdot 6H_2O$ (3.3 mmol), $FeCl_3 \cdot 6H_2O$ (7.7 mmol) and a quantity of mixture of $CoCl_2 \cdot 6H_2O$ and $ZnCl_2$ (the total amount of the two reagents was 5.5 mmol and the molar ratio of the two reagents were 1:0, 0.8:0.2, 0.6:0.4, 0.46:0.54, 0.44:0.56,) were dissolved in 80 mL deionized water under stirring to form a clear solution. Then the NaOH solution (0.5 mol L^{-1}, 150 mL) was gradually dropped into the previous metal salts solution with vigorous stirring for 30 min to form the precursor. The precursor was sealed in an autoclave and then heated to 250°C (heating rate: 2.3 °C min^{-1}) and maintained for 2 h, and subsequently allowed to cool to room temperature. The products were washed with deionized water and ethanol until neutral, and then dried at 60°C for 6 h in vacuum drying chamber.

Characterization

The crystalline structure was characterized by PANalytical Empyrean X-ray diffractometer (Netherlands) with Cu Kα radiation (λ=0.15406 nm). The elemental analysis was conducted by Shimadzu EPMA-1600 Electron-Probe Microanalyzer (Japan). The transmission electron microscope (TEM) images were obtained on a FEI Tecnai G2 F30 (USA). Magnetization curves were recorded at 25°C on a Jilin University JDM-13 vibrating sample magnetometer (China).

The Curie temperature was measured by thermogravimetric analysis (TGA) using Mettler-Toledo TGA 851 with an Nd-Fe-B magnet (100*50*5mm^3) placed over the nanoparticles at a distance about 10 cm. When the temperature is below the Curie temperature, the weights of nanoparticles recorded by TGA are less than the real weights due to the attractive magnetic force between nanoparticles and the magnet. When the increasing temperature reaches the Curie temperature, the nanoparticles will lose their magnetism and the weights recorded by TGA are equal to their real weights. The weight transition point recorded by TGA is referred to as the Curie temperature.

The time-dependent temperature curves of nanoparticle suspensions were determined by calorimetric measurements. The experimental setup is illustrated in **Fig. 1v**. To make the performance of nanoparticles under the alternating magnetic field closer to those used for clinical treatment, the experimental condition set was as that used in Jordan's clinical treatment. [26, 27] All the nanoparticles were decentralized into deionized water with the same concentration (112 mg ml^{-1}) and the frequency and intensity of the magnetic field set to 100 kHz and 200 Oe, respectively. Once irradiated, the temperature of suspension was measured by an alcohol thermometer at 60 s intervals.

Cell culture and cytotoxicity assay

Human epidermal keratinocyte (HaCaT) cells were purchased from China Center for Type Culture Collection (Wuhan) and maintained in high glucose Dulbecco's Modified Eagle Medium (DMEM) (Gibco, USA) in a humidified 37°C incubator (Thermos HERAcell150, USA) at 5% CO_2 supplemented with 10% fetal bovine serum (FBS) (Gibco, USA) and 1% penicillin-streptomycin (Gibco, USA). After sterilized with 75% (v/v) ethanol/ deionized water for 24 h and rinsed with phosphate buffer saline (PBS) three times, the particles were suspended in cell culture medium with a concentration of 0 μg ml^{-1}, 12.5 μg ml^{-1}, 25 μg ml^{-1}, 50 μg ml^{-1}, 100

μg ml^{-1} and 200 μg ml^{-1}. HaCat cells were seeded in 24-well plates and 96-well plates with a density of 5×10^4 cells ml^{-1} for evaluation of in vitro cytotoxicity of magnetic nanoparticles.

The quantitative evaluation of in vitro cytotoxicity of magnetic nanoparticles against HaCat cells were performed by using the cell counting kit-8 (CCK-8) assay (Dojindo Laboratories Kumamoto, Japan). HaCat cells were seeded in 96-well plates with a density of 5×10^4 cells ml^{-1}. After 3 h of culture, adherent cells were exposed to the fresh culture medium containing 0 μg ml^{-1} (control), 12.5 μg ml^{-1}, 25 μg ml^{-1}, 50 μg ml^{-1}, 100 μg ml^{-1} and 200 μg ml^{-1} nanoparticles. At 24 h, 48 h and 72 h, the cell viability was assessed. Briefly, the culture medium was refreshed and 10 μL CCK-8 was added to each well containing 100 μL new medium. After incubated in dark at 37 °C for 2 h, each set of nanoparticle solution of 100 μL was transferred to a new 96-well plate to measure the absorbance of the formazan product at 450 nm by using a microplate reader (SPECTRAFLUOR, TECAN, Sunrise, Austria). The cell viability was calculated using the formula (1):

$$Viability(\%)=[OD_{nanoparticles}-OD_{blank}]/[OD_{control}-OD_{blank}]\times100\% \quad (1)$$

Where $OD_{nanoparticles}$ is the optical density of the well containing various concentration of nanoparticles, DMEM medium and cells. $OD_{control}$ is the optical density of the well containing DMEM medium and cells. OD_{blank} is the optical density of the well only containing DMEM medium.

In addition, cell viability was observed by staining with Calcein-AM, Hoechst 33258, and propidium iodide (PI). After 72 h of culture, cells were rinsed with PBS for three times and stained with PBS containing 2 μmol L^{-1} Calcein-AM, 5 μg ml^{-1} Hoechst 33258, and 4 μmol L^{-1} PI (Sigma, Mo, USA). After incubation in dark at 37°C for 15 min, cells were rinsed with PBS for three times. Then the viable and dead cells were imaged using a fluorescent microscope (OLYMPUS BX71, Japan).

Results and Discussion

The size, morphology and crystalline information of the nanoparticle were investigated using TEM. All the nanoparticles are of regular tetragonal structure and the edge length of the tetragonal structure decreases with increasing Zn content. **Fig. 1a, 1e, 1i, 1m, 1q** shows the representative TEM images of $CoCr_{0.6}Fe_{1.4}O_4$, $Zn_{0.2}Co_{0.8}Cr_{0.6}Fe_{1.4}O_4$, $Zn_{0.4}Co_{0.6}Cr_{0.6}Fe_{1.4}O_4$, $Zn_{0.54}Co_{0.46}Cr_{0.6}Fe_{1.4}O_4$ and $Zn_{0.56}Co_{0.44}Cr_{0.6}Fe_{1.4}O_4$, respectively. To obtain the detailed crystalline information of particles, HRTEM and electron diffraction were performed. As **Fig. 1b, 1f, 1j, 1n, 1r** indicates, the interlayer distances are 0.489 nm, 0.251 nm, 0.238 nm, 0.295 nm and 0.256 nm, respectively, corresponding to (111), (311), (222), (220) and (311) lattice planes in spinel structure. In the electron diffraction images (**Fig. 1c, 1g, 1k, 1o, 1s**), the dense ring patterns match the standard body centered cubic spinel structure.

The XRD patterns of the nanoparticles are shown in **Fig. 1u**. All the patterns can be easily indexed to cubic spinel structure of $CoFe_2O_4$-$CoCrFe_2O_4$ (JCPDS-ICDD database 03-0864) and no obvious XRD peaks arising from impurities could be observed. A combination of TEM and XRD analyses confirms the spinel structure of the obtained particles. The element ratio in all nanoparticles was determined by Electron-Probe Microanalyzer. The results, together with the molar ratio of metal elements initially added, are given in supplementary materials (**Table S-1**†). Clearly, all metal elements in the nanoparticles do not deviate significantly from their initial stoichiometry. According to aforementioned experimental facts, it could be concluded that all the metal ions successfully enter into the lattice.

Fig. 1d, 1h, 1l, 1p, 1t depicts the edge length distributions of $CoCr_{0.6}Fe_{1.4}O_4$, $Zn_{0.2}Co_{0.8}Cr_{0.6}Fe_{1.4}O_4$, $Zn_{0.4}Co_{0.6}Cr_{0.6}Fe_{1.4}O_4$, $Zn_{0.54}Co_{0.46}Cr_{0.6}Fe_{1.4}O_4$, $Zn_{0.56}Co_{0.44}Cr_{0.6}Fe_{1.4}O_4$ nanoparticles and the mean edge length of the nanoparticles are found to be 139.8 nm, 67.3 nm, 32.2 nm, 30.3 nm and 25.1 nm respectively. Clearly, the edge length of the nanoparticles ranges from 20 nm to 200 nm and decreases with the increasing Zn content. The plausible interpretation is as follows. As the sum of the Zn^{2+} and Co^{2+} added is fixed, with the increasing quantity of Zn^{2+}, the quantity of $Zn(OH)_2$ will also rise and the $Co(OH)_2$ will drop in the precursor. Since the saturability of $Zn(OH)_2$ is much lower than the $Co(OH)_2$, the overall ions or ionomers content dissolved from the precursor into the solution will decrease. This decrease of dissolved ion content will inhibit the grain growth due to the deceleration of bulk and surface diffusion. [28]

The magnetic properties of these nanoparticles were investigated using vibrating sample magnetometer at room temperature (25 ^oC). **Fig. 2a** shows the detailed magnetization curves of the magnetic nanoparticles and its inset depicts the changes of H_c and saturation magnetization (M_s) against Zn content. As the content of Zn increases, the M_s increases initially and then experiences a decrease when the Zn content increases from 0.2 to 0.56. The magnetization of spinel cubic structure depends on the composition of cations in tetrahedral *A* site and octahedral *B* site. When Zn is added into the lattice, the non-magnetic Zn^{2+} tends to occupy tetrahedral sites by transferring Fe^{3+} to octahedral sites due to their preference by polarization effect, decreasing the magnetic moment of sub-lattice *A*. [29] The Fe^{3+} transferred from tetrahedral site to the octahedral site will lead to the increase of magnetic moment of sub-lattice *B*. The dominant *A*-*B* super-exchange interactions follow Neel's two sub-lattice model and the magnetic moment of the two sub-lattices are aligned approximately antiparallel to each other. [30] The net magnetic moment of the whole lattice is given by subtracting the magnetic moments of *A* sub-lattice from *B* sub-lattice. Therefore, the magnetization of the nanoparticles will increase with increasing Zn content, which may explain the observed initial increase of M_s.

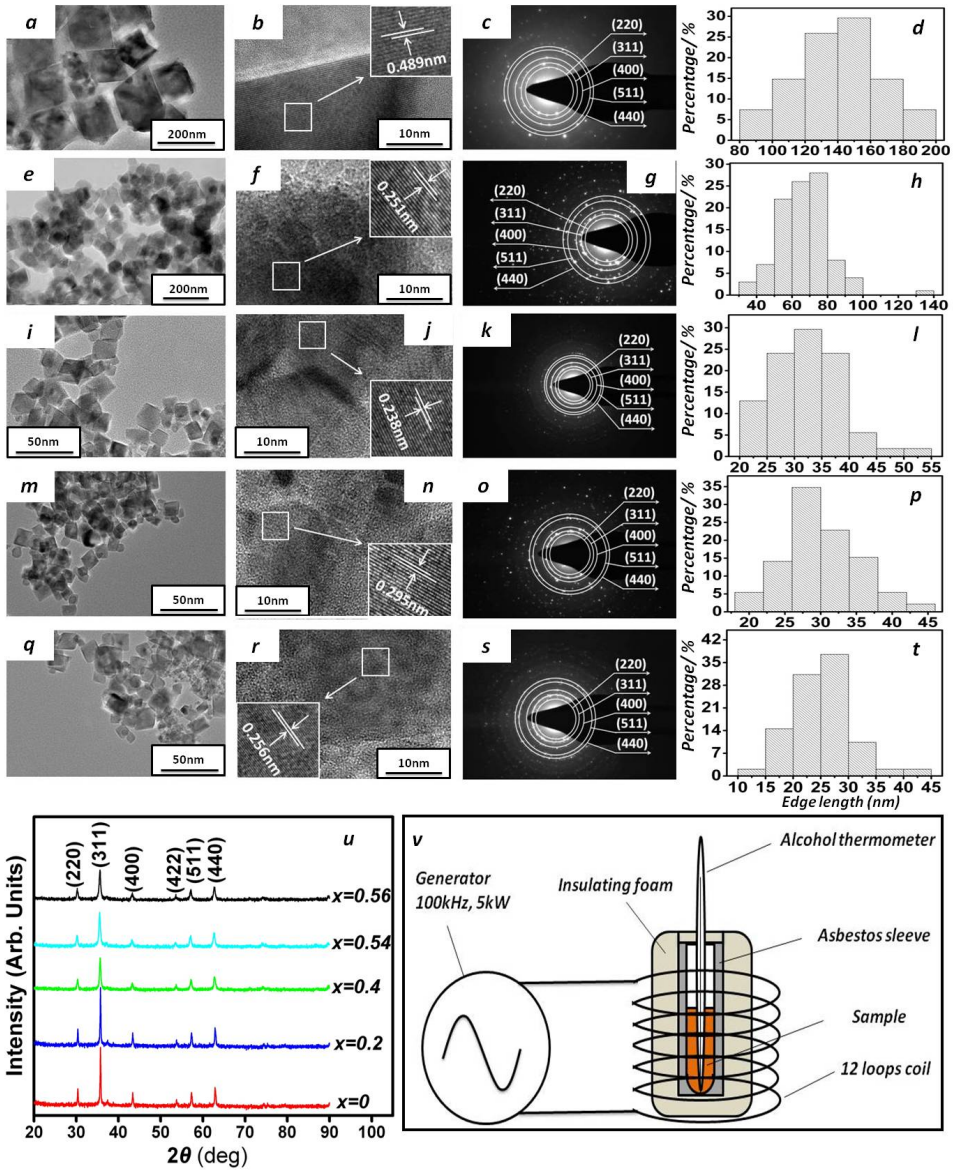

Fig. 1 TEM images, edge length distributions, XRD patterns and the experimental setup of calorimetric measurements of tetragonal $Zn_xCo_{1-x}Cr_{0.6}Fe_{1.4}O_4$ nanoparticles. $CoCr_{0.6}Fe_{1.4}O_4$: (a), (b), (c), (d); $Zn_{0.2}Co_{0.8}Cr_{0.6}Fe_{1.4}O_4$: (e), (f), (g), (h); $Zn_{0.4}Co_{0.6}Cr_{0.6}Fe_{1.4}O_4$: (i), (j), (k), (l); $Zn_{0.54}Co_{0.46}Cr_{0.6}Fe_{1.4}O_4$: (m), (n), (o), (p); $Zn_{0.56}Co_{0.44}Cr_{0.6}Fe_{1.4}O_4$: (q), (r), (s), (t). Among them, (a), (e), (i), (m) and (q) are TEM images; (b), (f), (j), (n) and (r) are HRTEM images; (c), (g), (k), (o) and (s) are electron diffraction images; (d), (h), (l), (p) and (t) are the statistical data of size distribution of each kind of nanoparticles obtained from 100 nanoparticles. (u) XRD patterns. (v) The experimental setup of calorimetric measurements.

When the content of Zn exceeds 0.2, the magnetic moment of the A site are decreased so much so that the dominant *A*-*B* super-exchange interactions become insignificant, with the *B*-*B* super-exchange interactions prevailing, which results in the random spin canting on *B* sites with respect to the direction of spins of the *A* site. [31] These canted spins lead to the decrease of the experimental value of M_s with the increasing concentration of Zn from 0.2 to 0.56. This process could be described by Yafet-Kittle (Y-K) model. According to the Y-K model, the existence of canted spins and their influence on magnetic moment can be observed by the Y-K angle ($\alpha_{Y\text{-}K}$) and its value could be calculated using the formula (2) [31]

$$n_B^e = M_B \cos\alpha_{Y\text{-}K} - M_A \qquad (2)$$

Where n_B^e ($n_B^e = M_W \cdot M_S/5585$, M_W is the molecular weight)

is the experimental magnetic moment expressed in the units of Bohr magneton, M_A and M_B are the Bohr magneton in the *A* sites and *B* sites. The calculated Y-K angles for each kind of nanoparticles are listed in **Table 1** and it is clear that the Y-K angle gradually increases with the increasing content of Zn. When the content of Zn is below 0.2, the Y-K angles are below 38°, and the substituting of a small quantity of Zn does not influence the sub-lattice interactions considerably and the Neel's two sub-lattice model is still valid. When the content of Zn is above 0.2, the Y-K angle gradually increases and finally extrapolates to 65.9° when the Zn content is 0.56. The substituting of large quantities of Zn content significantly influences the sub-lattice interactions and Neel's two sub-lattice model is invalid under this situation.

It is also observed that the increase of Zn^{2+} causes the decrease of H_c monotonously, which may result from the change of magnetocrystalline anisotropy. The change of magnetocrystalline anisotropy could be caused by the following two factors. a) Magnetic coupling. The replacement of Co^{2+} by Zn^{2+} weakens the magnetic coupling in the lattice, which may decrease the magnetocrystalline anisotropy and lead to lower H_c. b) Defects. There might be some defects in the nanoparticles generated in the synthesis process. The presence of defects such as point defects, dislocations, stacking faults, subgrain boundaries, inclusions and voids might affect the magnetocrystalline anisotropy. [32-34] These defects could affect magnetization in two ways. [35] First, they can act as centers for nucleation of new domain walls and aid magnetization reversal. This can occur at sites which locally have large demagnetizing fields due to shape irregularities, or at sites where the domain wall energy is locally changed by chemical or physical defects. Second, defects can pin existing domain walls and inhibit magnetization reversal by creating local energy barriers that impede wall movement. In the former case, defects would decrease magnetocrystalline anisotropy energy by creating a nucleation site, which could decrease H_c; whereas in the latter case, defects would increase magnetocrystalline anisotropy energy by pinning domain walls, which could increase H_c. It should be pointed out that, it is difficult to determine which type of defects and which way of affecting magnetization plays the prominent role, but their influence on H_c will be exerted by changing magnetocrystalline anisotropy. [36] In other words, the changes of magnetocrystalline anisotropy in this work might have the contribution of defects, although at current stage it is still hard to discern the mechanism.

The magnetocrystalline anisotropy constant in our work could be calculated by Brown's relation (3), [37]

$$H_c = 0.96K/Ms \qquad (3)$$

The magnetocrystalline anisotropy constant *K* of each kind of nanoparticles were calculated and given in **Table 1**. The magnetocrystalline anisotropy constant of each kind of nanoparticles decreases monotonically with the increasing content of Zn^{2+}, which accordingly gives rise to the decrease of H_c.

The thermogravimetric curves recorded are shown in **Fig. 2b.** As the temperature increases, the nominal weight decreases initially and then increases, which means that the magnetization of the nanoparticles increases firstly and decreases subsequently with the increasing temperature. A plausible interpretation is the following. The magnetic field intensity generated from Nd-Fe-B magnet is not high enough to make all the magnetic domains in the nanoparticles to be oriented in an ordered arrangement. The increase of temperature weakens the effect of domain wall pinning, [38] causing the increase of magnetic susceptibility and consequently the increase of magnetization. In addition, the nanoparticles under higher temperature have strong tendency to aggregate due to their high surface energy, resulting the reduction of surface area. [39, 40] Since the spin orientation at the surface is more easily disordered due to thermal fluctuations than those at the magnetic core, [28] the magnetic nanoparticles with lower surface area will have increased magnetization. When the temperature reaches the Curie temperature, the ordered arrangement of the magnetic domains in the nanoparticles will be completely destroyed and the magnetism of the nanoparticles will disappear. It is also observed that the temperature range of losing magnetization of the nanoparticles is broad. This is caused by the individual size differences of nanoparticles. According to Nikolaev's research, [41] the Curie temperature is directly proportional to the bulk density of exchange bonds. The surface layer thickness increases with the decreasing particle radius. Since the number of exchange bonds at the surface layer is less than that at the particle core, the smaller the magnetic nanoparticle size, the lower the Curie temperature. Thus, the temperature range of losing magnetization can also be influenced by the size distribution of nanoparticles, as shown in our work. When the temperature reaches the Curie temperature of a majority of nanoparticles, it will experience the most rapid weight increase in the curves and the Curie temperature could be determined by taking the maximum value of the first derivative of the thermogravimetric curves.

With the increasing content of Zn, the Curie temperature decreases monotonically, see **Fig. 2c (I)**. The Curie temperature of spinel ferrite nanoparticles mainly depends on the following two factors. a) The composition of cations in tetrahedral *A* site and octahedral *B* site, which determines the strength of super-exchange interaction of sub-lattices. When Zn is added into the lattice, the paramagnetic Zn^{2+} will cause the reduction of magnetic ions concentrations in *A* sites and reduce the dominant *A-B* super-exchange interactions and Curie temperature. [42, 43] b) Particle size. When Zn is added, smaller nanoparticles are generated due to the decrease of ions or ionomers content dissolved from the precursor into the solution. [18] Smaller particle size with a thicker surface layer would no doubt lead to lower Curie temperatures. [41] This also contributes to the observed decrease of the Curie temperature in this work. Compared with the nanoparticles without the substituting of Cr ($Zn_xCo_{1-x}Fe_2O_4$) in Arulmurugan's research (**Fig. 2c， II**), [22] the Curie temperature of $Zn_xCo_{1-x}Cr_{0.6}Fe_{1.4}O_4$ nanoparticles in our work decreases more significantly and in particular, the $Zn_{0.54}Co_{0.46}Cr_{0.6}Fe_{1.4}O_4$ nanoparticles with their Curie temperature about 45.7°C meets the requirements of self-regulating hyperthermia.

Table 1 The calculated magnetocrystalline anisotropy constant (*K*), Yafet-Kittle angle ($\alpha_{Y\text{-}K}$) and specific absorption rate (SAR) of each kind of nanoparticles

$Zn_xCo_{1-x}Cr_{0.6}Fe_{1.4}O_4$	$K(erg\ cm^{-3})$	$\alpha_{Y\text{-}K}$ (^{o})	$SAR(w\ kg^{-1})$
x=0	209848.8	22.19	29
x=0.2	129578.6	37.99	58
x=0.4	9302.8	53.24	145
x=0.54	1056.9	63.08	774
x=0.56	674.7	65.90	464

The time-dependent temperature curves of nanoparticle suspensions were determined by calorimetric measurements. All the nanoparticles were decentralized into deionized water with the same concentration (112 mg/mL) before exposure to the external alternating magnetic fields (200 Oe, 100 kHz), which is applicable to clinical therapy. As can be seen in **Fig. 2d**, after being irradiated for 60 mins, the temperature of suspension could rise to 28.5^{o}C ($CoCr_{0.6}Fe_{1.4}O_4$), 29.4^{o}C ($Zn_{0.2}Co_{0.8}Cr_{0.6}Fe_{1.4}O_4$), 31.6^{o}C ($Zn_{0.4}Co_{0.6}Cr_{0.6}Fe_{1.4}O_4$), 33.1^{o}C ($Zn_{0.56}Co_{0.44}Cr_{0.6}Fe_{1.4}O_4$) and 44.0^{o}C ($Zn_{0.54}Co_{0.46}Cr_{0.6}Fe_{1.4}O_4$). In order to evaluate heat efficiency quantitatively, specific absorption rate (SAR) under alternating magnetic fields, which describes the energy converted into heat per time and mass, was calculated using the formula (4): [44]

$$SAR=C(dT/dt)(m_s/m_m) \quad (4)$$

Where C is the specific heat capacity of suspension and its value is 4.18 J/gK; *dT/dt* is the initial slope of the time-dependent temperature curve; m_s is the mass of suspension and m_m is the mass of magnetic nanoparticles in the suspension. The calculated results are listed in **Table 1**. The SAR of $Zn_{0.54}Co_{0.46}Cr_{0.6}Fe_{1.4}O_4$ and $Zn_{0.56}Co_{0.44}Cr_{0.6}Fe_{1.4}O_4$ nanoparticles are 774 W kg^{-1} and 464 W kg^{-1} respectively which is at least 3 fold higher than the other three kinds of nanoparticles. The heat generation of nanoparticles in this work can be attributed to hysteresis loss. The H_c of $CoCr_{0.6}Fe_{1.4}O_4$, $Zn_{0.2}Co_{0.8}Cr_{0.6}Fe_{1.4}O_4$ and $Zn_{0.4}Co_{0.6}Cr_{0.6}Fe_{1.4}O_4$ nanoparticles are 6463 Oe, 3107 Oe and 342 Oe respectively, which are higher than the applied alternating magnetic field (200 Oe). This means that the saturated hysteresis loops cannot be completely used to generate heat. Unsaturated loops could be used，but will generate heat only at much reduced levels. [12] The *Hc* of the $Zn_{0.54}Co_{0.6}Cr_{0.6}Fe_{1.4}O_4$ and $Zn_{0.56}Co_{0.6}Cr_{0.6}Fe_{1.4}O_4$ nanoparticles are 174 Oe and 107 Oe which are lower than the applied alternating magnetic field (200Oe) This means that the hysteresis loops of these two kinds of nanoparticles could be completely used to generate heat and $Zn_{0.54}Co_{0.6}Cr_{0.6}Fe_{1.4}O_4$ nanoparticles with higher H_c and larger hysteresis loops will no doubt possess higher heat efficiency.

After a rapid increase of temperature, the $Zn_{0.54}Co_{0.6}Cr_{0.6}Fe_{1.4}O_4$ and $Zn_{0.56}Co_{0.6}Cr_{0.6}Fe_{1.4}O_4$ nanoparticle suspensions reach a stable temperature of 33.1^{o}C and 44.0^{o}C, which is close to their Curie temperatures, 34.3^{o}C and 45.7^{o}C, respectively. Only when the hyperthermia temperature is maintained below the Curie temperature, the nanoparticles will keep their magnetism and generate sufficient heat under an alternating magnetic field in this self-regulating system. Otherwise, the nanoparticles will lose their magnetism and will subsequently not generate heat, which makes these two suspensions remain constant around the Curie temperature of the custom-designed nanoparticles. It is striking to notice that the $Zn_{0.54}Co_{0.46}Cr_{0.6}Fe_{1.4}O_4$ nanoparticles with self-regulated temperature about 44.0^{o}C meets the requirement for hyperthermia.

A further requirement for medical applications involving novel nanoparticles is its biocompatibility. The cytotoxicity effects of $Zn_{0.54}Co_{0.46}Cr_{0.6}Fe_{1.4}O_4$ nanoparticles with concentrations of 0 μg ml^{-1}, 12.5 μg ml^{-1}, 25 μg ml^{-1}, 50 μg ml^{-1}, 100 μg ml^{-1} and 200 μg ml^{-1} on HaCaT cells was examined after growth in co-culture of 24 h, 48 h and 72 h. As shown in **Fig. 3a**, there is no significant difference in cell viability between all nanoparticle groups and control groups (p-value > 0.05). In order to have a more visualized observation of cell state, live-dead fluorescent microscopic analysis was performed. After the co-culture on HaCaT cells with $Zn_{0.54}Co_{0.46}Cr_{0.6}Fe_{1.4}O_4$ nanoparticles for 72 h, the cells were next stained with Calcein-AM, PI and Hochest 33258. Dead cells can then be identified by a red fluorescence generated by the PI after intercalating into DNA, which only occurs after the dead cell-permeable dye molecules enter the cell membrane. Cell nucleus can be identified by a blue fluorescence generated by Hochest 33258 after this living cell-permeable dye molecules bind to DNA. Living cells can be identified by a green fluorescence generated by the enzymatic hydrolysis of calcein-AM, which only occurs in living cells as a result of esterase activity. As can be seen in **Fig. 3b**, cells co-cultured with all the concentrations of nanoparticles for 72 h show calcein-positive, Hochest 33258-positive and PI-negative state. The results, together with CCK-8 assay suggest the low cytotoxicity of $Zn_{0.54}Co_{0.46}Cr_{0.6}Fe_{1.4}O_4$ nanoparticles.

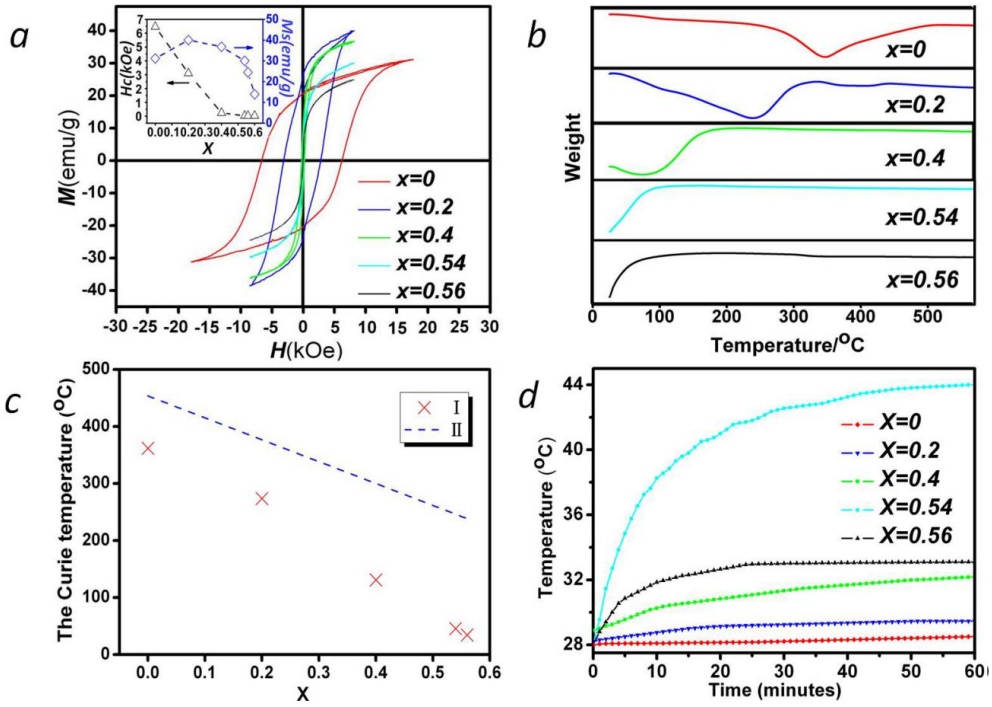

Fig 2. Magnetic properties of $Zn_xCo_{1-x}Cr_{0.6}Fe_{1.4}O_4$ nanoparticles. (a) Magnetization curves and the changes of H_c and M_s against the content of Zn (Inset). The M_s increases initially with the content of Zn increasing from 0 to 0.2, and then experiences a decrease with the content of Zn increasing from 0.2 to 0.56, H_c decreases monotonously, from 6400 Oe to 107 Oe. (b) The thermogravimetric curves of nanoparticles. As the temperature increases, the nominal weight decreases initially and then increases. (c) The Curie temperature against the Zn content (I) and a fitted curve of Arulmurugan's work (II), see supplementary materials (Fig. S-1†). With the increasing content of Zn, Curie temperature of nanoparticles in our work decreases monotonically, from 361.7°C to 34.3°C. (d) Time-dependent temperature curves of nanoparticles in 100 kHz and 200 Oe alternating magnetic field. $Zn_{054}Co_{0.46}Cr_{0.6}Fe_{1.4}O_4$ nanoparticles with Curie temperature at 45.7°C and H_c at 174 Oe result in the self-regulating temperature of nanoparticles suspension at hyperthermia temperature (around 44.0°C) with SAR at 774 W kg^{-1}

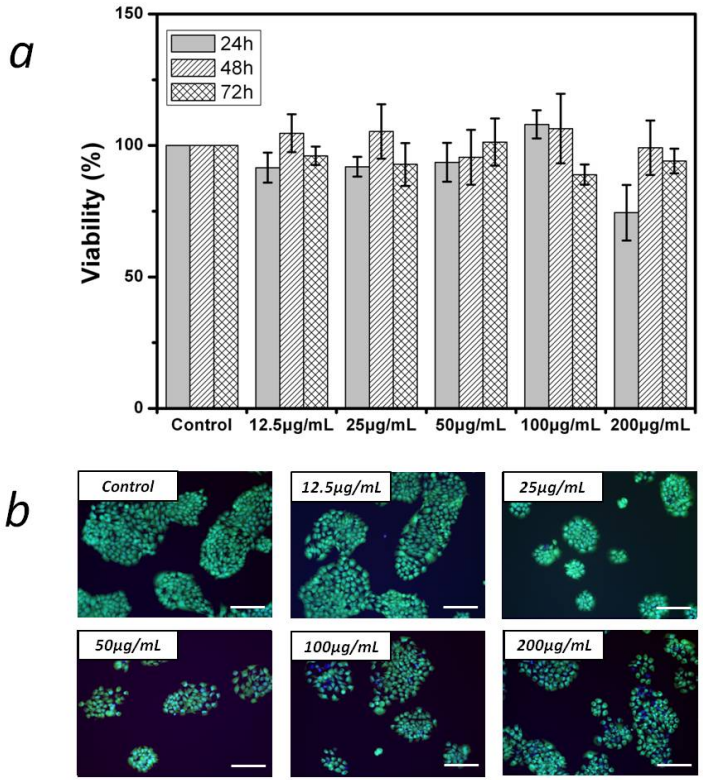

Fig 3. Effects of $Zn_{0.54}Co_{0.46}Cr_{0.6}Fe_{1.4}O_4$ nanoparticles on the viability of Hacat cells. (a) Cell viability was assessed by CCK-8 assay at 24 h, 48 h and 72 h after co-culture with various concentrations of $Zn_{0.54}Co_{0.46}Cr_{0.6}Fe_{1.4}O_4$ nanoparticles. Values were represented as the percentages of cell viability compared with that of the control group and expressed as means±standard deviation of triplicate determinations. (b) Representative fluorescent images of detached Hacat cells which are triple stained with calcein-AM (green), PI (red) and Hochest (blue) after co-culture with various concentrations of $Zn_{0.54}Co_{0.46}Cr_{0.6}Fe_{1.4}O_4$ nanoparticles for 72 h. Scale bar: 50 μm.

Conclusions

In summary, optimizing the Curie temperature and coercivity of Co-Zn ferrite nanoparticles allows for the custom design of self-regulating hyperthermia nano-vehicles by substituting a pre-determined quantity of Cr^{3+} through a hydrothermal process. Regular tetragonal morphology nanoparticles with Curie temperature from 361.7 ^oC to 34.3 ^oC and H_c from 6400 Oe to 107 Oe were obtained. Among them, the Curie temperature and H_c of $Zn_{0.54}Co_{0.46}Cr_{0.6}Fe_{1.4}O_4$ nanoparticles reach 45.7^oC and 174 Oe respectively. The temperature of these nanoparticles suspension can be self-regulated at 44.0^oC, close to but critically under the clinically used magnetic fields. The evaluation of in vitro cytotoxicity of $Zn_{0.54}Co_{0.46}Cr_{0.6}Fe_{1.4}O_4$ nanoparticles also suggests low toxicity. This study provides reference information for the custom synthesis of a novel magnetic nanoparticle which in the future could be used in cancer therapeutics for precise energy transfer from the external magnetic field to the tumor via a self-regulating delivery system to be used in hyperthermia. The data shows the bespoke synthesis of nanoparticles to provide the necessary physical platform to regulate not just the Curie temperature, but also the coercivity by a change in the microstructure.

Acknowledgements

The NSFC (11572080) and National Basic Research Program of China (2015CB057306) were acknowledged for the financial support.

References

1 R. K. Gilchrist, R. Medal, W. D. Shorey, R. C. Hanselman, J. C. Parrott and C. B. Taylor, *Ann. Surg.,* 1957, **146**, 596-606.
2 A. Bianco, K. Kostarelos and M. Prato, *Curr. Opin. Chem. Biol.,* 2005, **9**, 674-679.
3 E. Heister, V. Neves, C. Lamprecht, S. R. P. Silva, H. M. Coley and J. McFadden, *Carbon*, 2012, **50**, 622-632.
4 E. Heister, C. Lamprecht, V. Neves, C. Tilmaciu, L. Datas, E. Flahaut, B. Soula, P. Hinterdorfer, H. M. Coley, S. R. P. Silva and J. McFadden, *ACS Nano*, 2010, **4**, 2615-2626.
5 A. Jordan, R. Scholz, P. Wust, H. Fähling and R. Felix, *J. Magn. Magn. Mater.,* 1999, **201**, 413-419.
6 K. Overgaard and J. Overgaard, *Eur. J. Cancer*, 1972, **8**, 65-78.
7 M. Hiraoka, S. Jo, K. Akuta, Y. Nishimura, M. Takahashi and M. Abe, *Cancer*, 1987, **60**, 121-127.
8 T. Miyagawa, H. Saito, Y. Minamiya, K. Mitobe, S. Takashima, N. Takahashi, A. Ito, K. Imai, S. Motoyama and J. Ogawa, *Int. J. Clin. Oncol.,* 2014, **19**, 722-730.
9 V. Herynek, K. Turnovcová, P. Veverka, T. Dědourková, P. Žvátora, P. Jendelová, A. Gálisová, L. Kosinová, K. Jiráková and E. Syková, *Int. J. Nanomedicine*, 2016, **11**, 3801-3811.
10 E. Natividad, M. Castro, G. Goglio, I. Andreu, R. Epherre, E. Duguet and A. Mediano, *Nanoscale*, 2012, **4**, 3954-3962.
11 I. Astefanoaei, I. Dumitru, H. Chiriac and A. Stancu, *J. Appl. Phys.,* 2014, **115**, 17B531.
12 R. Miyamoto, H. Saito, M. Suzuki, N. Yoshimura and K. Mitobe, *Electr. Commun. Jpn.,* 2016, **99**, 55-62.
13 S. Vasseur, E. Duguet, J. Portier, G. Goglio, S. Mornet, E. Hadová,
28 P. Bennema, *J. Cryst. Growth*, 1969, **5**, 29-43.
29 M. Ajimal and A. Maqsood, *Mater. Lett.,* 2008, **62**, 2077-2080.
30 S. M. Patange, S. S. Desai, S. S. Meena, S. M. Yusuf and S. E. Shirsath, *RSC Adv.,* 2015, **5**, 91482-91492.
31 R. Topkaya, A. Baykal and A. Demir, *J. Nanopart. Res.,* 2013, **15**, 1-18.
32 F. D. Stacey and K. N. Wise, *Austr. J. Phys.,* 1967, **20**, 507-514.
33 D. J. Dunlop, *Earth Planet Sci. Lett.,* 1986, **78**, 288-295.
34 F. Heider, D. J. Dunlop and N. Sugiura, *Science*, 1987, **236**, 1287-1290.
35 B. Moskowitz, *J. Geophys. Res.,* 1993, **98**, 18011-18026.
36 W. S. Chiu, S. Radiman, R. Abd-Shukor, M. H. Abdullah and P. S. Khiew, *J. Alloy. Compd.,* 2008, **459**, 291-297.
37 H. Yang, Z. Wang, L. Song, M. Zhao, J. Wang and H. Luo, *J. Phys.*
K. Knížek, M. Maryško, P. Veverka and E. Pollert, *J. Magn. Magn. Mater.,* 2006, **302**, 315-320.
14 U. Gneveckow, A. Jordan, R. Scholz, V. BRüSS, N. Waldöfner, J. Ricke and P. Wust, *Med. Phys.,* 2004, **31**, 1444-1451.
15 Q. A. Pankhurst, J. Connolly, S. K. Jones and J. J. Dobson, *J. Phys. D Appl. Phys.,* 2003, **36**, R167.
16 R. A. Bohara, N. D. Thorat, A. K. Chaurasia and S. H. Pawar, *RSC Adv.,* 2015, **5**, 47225-47234.
17 V. Mameli, A. Musinu, A. Ardu, G. Ennas, D. Peddis, D. Niznansky, C. Sangregorio, C. Innocenti, Nguyen T. K. Thanh and C. Cannas, *Nanoscale*, 2016, **8**, 10124-10137.
18 M. Veverka, K. Závěta, O. Kaman, P. Veverka, K. Knížek, E. Pollert, M. Burian and P. Kašpar, *J. Phys. D Appl. Phys.,* 2014, **47**, 065503.
19 I. Sharifi and H. Shokrollahi, *J. Magn. Magn. Mater.,* 2012, **324**, 2397-2403.
20 R. Arulmurugan, G. Vaidyanathan, S. Sendhilnathan and B. Jeyadevan, *Physica B*, 2005, **363**, 225-231.
21 W. Zhang, X. Zuo, D. Zhang, C. Wu and S. R. P. Silva, *Nanotechnology*, 2016, **27**, 245707.
22 M. A. Gabal, Y. M. Al Angari and F. A. Al-Agel, *J. Mol. Struct.,* 2013, **1035**, 341-347.
23 A. A. Birajdar, S. E. Shirsath, R. H. Kadam, S. M. Patange, K. S. Lohar, D. R. Mane and A. R. Shitre, *J. Alloy. Compd.,* 2012, **512**, 316-322.
24 B. M. Sass and D. Rai, *Inorg. Chem.,* 1987, **26**, 2228-2232.
25 M. Johannsen, U. Gneveckow, L. Eckelt, A. Feussner, N. Waldöfner, R. Scholz, S. Deger, P. Wust, S. A. Loening and A. Jordan, *Int. J. Hyperther.,* 2005, **21**, 637-647.
26 M. Johannsen, U. Gneveckow, B. Thiesen, K. Taymoorian, C. H. Cho, N. Waldöfner, R. Scholz A. Jordan, S. A. Loening and P. Wust, *Eur. Urol.,* 2007, **52**, 1653-1662.
27 K. Maier-Hauff, F. Ulrich, D. Nestler, H. Niehoff, P. Wust, B. Thiesen, H. Orawa, V. Budach and A. Jordan, *J. Neuro-oncol.,* 2011, **103**, 317-324.

D Appl. Phys., 1996, **29**, 2574.
38 P. Gaunt, *Philos. Mag. B*, 1983, **48**, 261-276.
39 N. A. Frey, S. Peng, K. Cheng and S. Sun, *Chem. Soc. Rev.* 2009, **38**, 2532-2542.
40 C. T. Campbell, S. C. Parker and D. E. Starr, *Science*, 2002, **298**, 811-814.
41 V. I. Nikolaev and A. M. Shipilin, *Phys. Solid State*, 2003, **45**, 1079-1080.
42 T. Upadhyay, R. V. Upadhyay, R. V. Mehta, V. K. Aswal and P. S. Goyal, *Phys. Rev. B*, 1997, **55**, 5585.
43 R. Arulmurugan, B. Jeyadevan, G. Vaidyanathan and S. Sendhilnathan, *J. Magn. Magn. Mater.,* 2005, **288**, 470-477.
44 I. Hilger, K. Frühauf, W. Andrä, R. Hiergeist, R. Hergt and W. A. Kaiser, Acad. Radiol., 2002, **9**, 198-202.